Angle-resolved electron energy loss spectroscopy of valence-shell and Si 2*p* pre-edge excitation of SiF_4: Bethe surface and absolute generalized oscillator strength measurement

X. W. Fan and K. T. Leung[a)]
Department of Chemistry, University of Waterloo, Waterloo, Ontario N2L 3G1, Canada

(Received 23 February 2001; accepted 17 May 2001)

Absolute generalized oscillator strengths (GOSs) of discrete transitions in the preionization-edge region of the valence and Si 2*p* inner shells of SiF_4 have been determined as functions of energy loss and momentum transfer by using angle-resolved electron energy loss spectroscopy at 2.5 keV impact energy. The GOS profiles of the pre-edge features are generally consistent with the spectral assignments based on the term values of the virtual and Rydberg states from earlier valence and inner-shell studies. In particular, the GOS profiles for these low-lying preionization-edge features in the valence shell are found to be dominated by a strong maximum at zero momentum transfer, consistent with the proposed assignment of predominantly dipole-allowed Rydberg and mixed valence-Rydberg transitions. In the case of the lowest-lying preionization-edge $1t_1 \rightarrow 6a_1$ feature, which is formally dipole-forbidden, the present work shows that such a shape for the GOS profile is, however, not exclusive to just dipole-allowed transitions. In the Si 2*p* shell, the GOS profiles for the well resolved, intense σ^* resonance and three higher-lying Si 2*p* pre-edge features have been determined and are found to be largely dominated by dipole-allowed (Rydberg) excitations. Differences in and between the GOS profiles for the valence-shell and Si 2*p* pre-edge features in SiF_4 are identified. No discernible secondary extrema can be found in any of these GOS profiles. The present GOS results for SiF_4 are compared with those reported for other cage-like molecules, including CF_4 and SF_6. © *2001 American Institute of Physics.* [DOI: 10.1063/1.1384457]

I. INTRODUCTION

In the past two decades, optical electronic spectroscopy continues to focus on the precise determination of the energies of electronic states while the progress on the measurement of transition probabilities or oscillator strengths (OSs) remains largely limited. In spite of the advent of synchrotron radiation research, accurate measurement of absolute dipole OS remains to be a major challenge for photoabsorption and other electronic spectroscopic methods, principally due to the bandwidth/linewidth limitations intrinsic in the use of the Beer–Lambert law for discrete transitions[1] and the practical difficulties of measuring over a wide photon energy range.[2] Even given the generally lower resolving power, zero-degree (i.e., forward) electron scattering techniques at negligible momentum transfer[2] have two fundamental advantages over photoabsorption methods for determining dipole OSs. These are the collection of the precise absolute cross sections (oscillator strength) data over a wide energy range without performing an ''absolute'' experiment and avoidance of the difficulties associated with the use of the Beer–Lambert law.[1] In addition nonoptical electronic processes, not governed by the dipole selection rules,[3,4] can be observed if the electron scattering intensities are studied as a function of scattering angle away from zero degree. The concept of generalized oscillator strength (GOS) was first introduced to electron scattering by Bethe[5] and later elaborated in detail by Inokuti.[6] Over three decades ago, Lassettre and co-workers pioneered the use of angle-resolved electron energy loss spectroscopy (EELS) for accurate determination of absolute dipole OS by extrapolating precise GOS measurements to the optical limit.[3] In the past several years, angle-resolved EELS has been used in our laboratory to study the electronic structures of the valence and inner shells of a number of polyatomic molecules, particularly chlorofluorocarbons $CF_{4-n}Cl_n$ $(n=0-4)$[7–10] and their chlorofluorohydrocarbon homologs, $CHF_{3-m}Cl_m$ $(m=1-3)$.[11–13] A recent review of our work and this particular area has been given by Leung.[14] Very recently, we have extended our investigation to electronic excitations in the outer-core shells of Ar[15] and the autoionization resonances in Ar[16] and He.[17]

As one of the by-products in plasma etching of silicon commonly employed in the microelectronics and semiconductor industry, silicon tetrafluoride (SiF_4) is one of the more relevant technological silicon compounds. Along with SF_6,[18,19] SiF_4 belongs to an important group of popular model compounds useful for studying the so-called ''caged'' effects, particularly related to the continuum or shape resonances. The valence and Si 2*p* inner-shell electronic structures of SiF_4 have been studied extensively by a variety of techniques, including photoabsorption[20–26] and small-angle electron scattering techniques.[27,28] These ''optical'' studies have largely focused on the dipole OS in the discrete and continuum regions as well as the spectral assignments of the

a)Electronic mail: tong@uwaterloo.ca

electronic transitions in the valence and Si $2p$ shells (under the dipole selection rules). The present work, on the other hand, provides a new measurement of the absolute GOS profiles for several low-lying preionization-edge transitions in the valence and Si $2p$ shells of SiF_4, which may be used to provide further insights into the electron-impact excitations of ''caged'' compounds. These results on SiF_4 will also be compared with our earlier angle-resolved EELS data on SF_6[18] and its valence-isoelectronic homologs, CF_4 and CCl_4.[7]

II. EXPERIMENTAL METHOD

Our recently improved apparatus and the experimental procedure used for the present angle-resolved EELS study have been described in detail elsewhere.[15] Briefly, a collimated electron beam was accelerated to 2.5 keV impact energy and crossed with a gas jet expanded from a nozzle (0.5 mm diameter) positioned at 1 cm above the collision center. The transfer of energy and momentum from the incident electron promotes the gaseous target from its electronic ground state (M) to an excited state (M^*),

$$e^-(E_0,\mathbf{k}_0)+M\rightarrow e^-(E_0-E,\mathbf{k})+M^*, \tag{1}$$

where E_0 (or E_0-E) and $\mathbf{k}_0$ (or $\mathbf{k}$) are the kinetic energy and momentum of the incident (or scattered) electron, respectively. Electrons scattered with an energy loss E at a scattering angle θ (from the forward direction) were analyzed using a hemispherical energy analyzer equipped with a seven-element input lens. The magnitude of the momentum transfer $\mathbf{K}$ $(=\mathbf{k}_0-\mathbf{k})$ is related to the scattering angle θ by $K^2=k_0^2+k^2-2k_0k\cos\theta$. The intensity of the scattered electron with an energy loss E at a scattering angle θ is proportional to the differential cross section $d^2\sigma/d\Omega\, dE$. Angle-resolved EELS spectra of the sample gas introduced to the center of the collisional cell (sample spectra) were collected at a series of θ angles (corresponding to different momentum transfers) sequentially in repetitive scans. After each measurement of the sample spectra, an identical set of EELS spectra of the sample gas introduced outside the collision cell at the same pressure $(1-2\times10^{-5}$ Torr) were recorded in the same energy loss and angular ranges (ambience spectra). Contributions from the ambient gas were removed by subtracting the corresponding ambience spectra from the sample spectra after appropriate normalization. This correction of the ambience contribution is crucial to assuring precise GOS measurement especially for inner-shell and other transitions with low cross sections.

For high-energy electron collisions, the influence of the incident electron upon the target can be regarded as a sudden and impulsive encounter. Under these conditions (and after the EELS spectra have been relatively normalized to one another), the differential cross section can be converted (in the first Born approximation) to the differential GOS, $df(K,E)/dE$, by using the Bethe–Born formula (in Rydberg atomic units):[6]

$$\frac{df(K,E)}{dE}=\frac{k_0}{k}K^2\frac{E}{4}\frac{d^2\sigma}{d\Omega\, dE}, \tag{2}$$

where $d\Omega$ corresponds to the detection solid angle. The GOS, $f(K,E)$, is defined as

$$f(K,E)=\frac{E}{K^2}\left|\left\langle\Psi_n\left|\sum_{j=1}^{N}\exp(i\mathbf{K}\cdot\mathbf{r}_j)\right|\Psi_0\right\rangle\right|^2, \tag{3}$$

where Ψ_0 and Ψ_n are the (N-electron) electronic wave functions of the initial and final states, respectively, and $\mathbf{r}_j$ is the position of the jth electron with respect to the center-of-mass of the target. The GOS at any K value can be made absolute independently by using the Bethe sum rule:[6]

$$\int\frac{df(K,E)}{dE}dE=N, \tag{4}$$

where N is the total number of electrons in the target. In the Bethe-sum-rule normalization procedure, the intensity of the relative GOS obtained at a particular momentum transfer is first numerically integrated over a sampling energy loss range of 100 eV. The remaining intensity of the valence shell above 100 eV for SiF_4 is estimated by integration of a fitted function $B(E)=a/E^{1.5}+b/E^{2.5}+c/E^{3.5}$ from 100 eV to infinity, where the empirical constants a, b, and c are obtained by curve-fitting $B(E)$ to the experimental data in the energy loss range of 70–100 eV. The sum of these two integrated intensities is then normalized to the integrated oscillator strength of 33.4, which corresponds to the total number of valence-shell electrons (32), plus an appropriate correction of the contribution due to Pauli-excluded transitions from other inner shells (1.4).[29,30]

For angle-dependent studies that involve finite momentum transfers, Lassettre and co-workers[31] have shown that the GOS for a bound-state excitation can be expanded as an even power series of K (the so-called Lassettre series):

$$f(K,E)=\frac{1}{(1+x)^6}\sum_{n=0}^{m}f_n\left(\frac{x}{1+x}\right)^n;\quad 2\leqslant m\leqslant 5, \tag{5}$$

where $x=K^2/(\sqrt{2I}+\sqrt{2|I-W|})^2$, I is the ionization potential, and W is the excitation energy of the discrete transition. The integer m $(=3$ in the present expansion) is chosen according to the amount of available data points and the accessible experimental range of momentum transfer. In the limit when K approaches zero, the GOS approaches the dipole OS, f_0. The original Lassettre series has been used quite successfully for a quantitative estimate of the dipole OS by extrapolating the measured GOS data to zero momentum transfer. The other parameters f_n in the Lassettre series are related to linear combinations of the respective multiple matrix elements and can be used to characterize the nature of the underlying excitation.[3,32]

Silicon tetrafluoride (99.99% purity) was purchased from Matheson and used without further purification. Our

spectrometer was operated routinely with an energy resolution of 0.8 eV full-width at half-maximum (FWHM) and an angular resolution of 0.2° half-angle. The energy and angular scales have been calibrated by using standard procedures as discussed previously.[15,19] No geometrical correction was found to be necessary for the small experimental angular range and the high impact energy employed in the present work.

III. RESULTS AND DISCUSSION

A. Overview of the electronic structure of valence and Si 2*p* shells in SiF_4

Silicon tetrafluoride is a 50-electron system with a T_d molecular symmetry. In accord with the photoelectron data,[33,34] the single-electron configuration for the ground electronic state of SiF_4 can be written as

$$\underbrace{1a_1^2}_{\text{Si } 1s}\ \underbrace{1t_2^6 2a_1^2}_{\text{F } 1s}\ \underbrace{3a_1^2}_{\text{Si } 2s}\ \underbrace{2t_2^6}_{\text{Si } 2p}\ \underbrace{4a_1^2 3t_2^6}_{\text{Inner-valence}}\ \underbrace{5a_1^2 4t_2^6 1e^4 5t_2^6 1t_1^6(\text{HOMO})}_{\text{Outer-valence}}\ \text{Occupied orbitals}$$

$$\underbrace{6a_1^0(\text{LUMO})6t_2^0 2e^0 7t_2^0}_{\text{Virtual}}\ \text{Unoccupied orbitals}$$

The vertical ionization potentials for the removal of the outer-valence molecular orbitals (MOs)[34] and the energies for the main ionic states of the inner-valence orbitals,[35] as well as the term values for the unoccupied virtual MOs and Rydberg orbitals are summarized in Table I. Figure 1(a) compares our EELS spectrum for the valence-shell region (up to 100 eV) measured at 1.5° (from the forward scattering direction) with the photoabsorption spectrum determined by Suto *et al.*[20] and with the zero-angle EELS spectrum obtained by Guo *et al.*[27] after corrected by a multiplication factor of 1.23, as suggested by Olney *et al.*[2] Excellent agreement is found between the earlier published photoabsorption[20] and the corrected zero-angle EELS spectrum.[27] Despite the somewhat lower energy resolution used in the present work, there is general accord in the shape among all three spectra. The overall intensity of our EELS spectrum measured at 1.5° is found to be generally lower than the other two spectra, which is consistent with the predominantly dipole nature of the excitation/ionization processes in SiF_4. These spectra reveal a prominent peak at 13.0 eV along with two other discernible features converging to the first ionization threshold, the $X(1t_1)^{-1}$ state. Above the ionization threshold, the absorption spectrum follows the ''generic'' pattern of a rising band followed by a falling tail. Due to the complexities in this region, excitation spectroscopy such as photoabsorption and EELS would not be the best tool to decipher the multitude of electronic excitation and ionization structures. In the present work we therefore focus primarily on the preionization-edge discrete excitation features and their assignments will be discussed in more detail in Sec. III C.

Figure 1(b) shows our EELS spectrum for the Si L-edge region (100–190 eV) measured at 1.5°, along with the photoabsorption spectrum of Friedrich *et al.*[23] and the zero-angle EELS spectrum of Guo *et al.*[28] after the appropriate correction, as suggested by Olney *et al.*[2] The small discrepancies between the photoabsorption and zero-angle EELS spectra may likely be related to background correction and/or normalization, which tends to accentuate the weak inner-shell region. The present result appears to be consistent with the corrected zero-angle EELS spectrum of Guo *et al.*[28] after due consideration is given to the reduction in the GOS of the predominantly dipole-allowed structure with an increasing scattering angle. Below the ionization edges of Si $2p_{3/2}$ at 111.7 eV and Si $2p_{1/2}$ at 112.3 eV, there are no intense peak (doublet) at 106.4 eV, commonly known as the σ^* resonance, and a broader band centered at 109.5 eV in our spectrum, which can be further resolved into several peaks (including individual spin–orbit components) in the reported photoabsorption[23] and zero-angle EELS spectra.[28] Further details of their assignments are given in Sec. III D. On the other hand, the prominent peak at 117.5 eV and the broad band centered at 132.5 eV found in the continuum cannot be resolved further. Both of these features are characteristic of continuum or shape resonances. In particular, the post-edge feature located at 117.5 eV has been assigned as an e shape resonance associated with transitions to quasi-bound states in the continuum induced by the electronegative F ligands, while the band at 132.5 eV can be described as a t_2 shape resonance or alternatively an atomic-like delayed onset phenomenon.[25,28] Finally, a broad band is also found at ~160 eV and it can generally be attributed to pre-edge excitations converging to the Si *2s* ionization edge at 163.7 eV.

B. Bethe surface of the valence shell

Figure 2 shows the EELS spectra of the valence shell of SiF_4 collected in steps of 0.5° from 1.5° to 9.5° in the form of a Bethe surface plot. These EELS spectra have been obtained relatively normalized to one another and made absolute using the Bethe sum rule. In the framework of the first

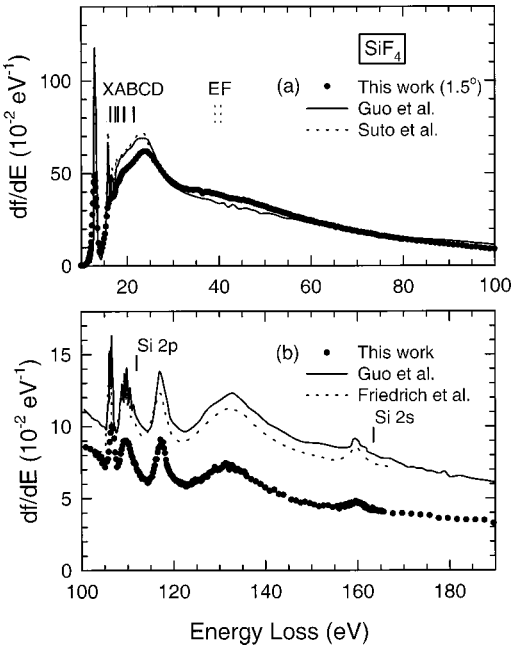

FIG. 1. Absolute electron energy loss spectra of (a) the valence shell and (b) Si $2p$ and $2s$ shells of SiF_4 measured at 1.5° and 2.5 keV impact energy. (a) The valence-shell spectrum is compared with the photoabsorption spectrum determined by Suto *et al.* (Ref. 20) and the zero-angle EELS spectrum obtained by Guo *et al.* (Ref. 27) after corrected by a multiplication factor of 1.23 as suggested by Olney *et al.* (Ref. 2). The vertical ionization potentials for the outer-valence ionic states: $X(1t_1)^{-1}$, $A(5t_2)^{-1}$, $B(1e)^{-1}$, $C(4t_2)^{-1}$, and $D(5a_1)^{-1}$ and the energies for the main-line inner-valence ionic states $E(3t_2)^{-1}$ and $F(4a_1)^{-1}$ are obtained from the photoelectron data of Yates *et al.* (Ref. 34) and Perry and Jolly (Ref. 35), respectively. (b) The electron energy loss spectrum for the Si $2p$ and $2s$ shells is compared with the photoabsorption spectrum of Friedrich *et al.* (Ref. 23) and the zero-angle EELS spectrum of Guo *et al.* (Ref. 28) after the appropriate correction recommended by Olney *et al.* (Ref. 2). The ionization potentials of the Si $2p_{3/2}$, $2p_{1/2}$, and $2s$ edges are 111.7 eV, 112.3 eV, and 163.7 eV, respectively.

Born scattering theory, the Bethe surface is a three-dimensional representation of the GOS as a function of energy loss and the logarithm to the base e of the square of the momentum transfer. The Bethe surface contains all the information about the inelastic electron scattering process with an atom or molecule, and can be used for analyzing such quantities as stopping power, total inelastic scattering cross section, the Compton profile, and polarizability.[6] The Bethe surface can be generally divided into two kinematical domains: dipole-scattering and impact-scattering. For ''distant'' collisions, which are mainly governed by dipole interaction, the corresponding dipole-scattering domain of small momentum transfer and energy loss exhibits sharp ''optical'' features found in the valence shell [Fig. 2(b)]. On the other hand, the impact-scattering domain of large momentum transfer and energy loss (which corresponds to the kinematical region for ''close'' collisions) reveals a weak broad ridge that disperses to a higher energy loss with increasing momentum transfer [Fig. 2(a)]. This ridge is the result of momentum conservation in the inelastic electron–molecule collision and becomes the well-known Bethe ridge in the Born approximation. The energy dispersion of this ridge with respect to K is generally related to manifestation of different Fourier-transform components of the overlap density between the initial-state and final-state wave functions.[6]

It is of interest to compare the Bethe surface of SiF_4 (Fig. 2) with our earlier angle-resolved EELS data for other ''cage-like'' valence-isoelectronic homologs with T_d symmetry, CF_4 and CCl_4.[7] In particular, the preionization-edge features of SiF_4 are clearly different from that of CF_4, reflecting the differences in the nature of the electronic structures in the two molecules. Above the ionization edge, the Bethe surface of SiF_4 resembles that of CF_4, despite the somewhat lower absolute intensity in SiF_4. Furthermore, unlike CCl_4, the Bethe surfaces of SiF_4 and CF_4 are noticeably less concentrated in the dipole-scattering region and are more extended above 40 eV energy loss. It is not surprising that the Bethe surfaces of SiF_4 and CF_4 are similar to each other because the primary differences between the valence shells of the two molecules are in the nature of the atomic orbitals in the central atoms used for forming the MOs. Although the Si $3p$ and $3s$ atomic orbitals in SiF_4 possess an additional radial node and are somewhat more diffuse and spatially extended relative to the corresponding C $2p$ and $2s$ orbitals in CF_4,[7] it is insufficient to produce significant changes in the spatial distributions of the valence-shell electron densities (and hence the ionization potentials of the outer-valence orbitals that are heavily based on the atomic orbitals of the ligands). The sizes of the valence shells of SiF_4 and CF_4 are therefore

TABLE I. Experimental vertical ionization potentials (IPs) of the occupied valence orbitals and term values of the unoccupied virtual and Rydberg orbitals in SiF_4.

Occupied orbital	IP (eV) Ref. 34	Unoccupied orbital	Term value (eV) Ref. 20	Ref. 27	Ref. 28	Ref. 23
$1t_1$ (HOMO)	16.4	$4p$	–	–	1.11–1.20	–
$5t_2$	17.5	$3d$	1.60–1.94	1.56–1.74	1.79–1.81	1.5
$1e$	18.1	$4s$	–	1.56–1.74	1.79–1.81	2.2
$4t_2$	19.4	$3p$	3.22–3.47	2.43–2.64	2.34–2.40	–
$5a_1$	21.5	$3s$	4.62–4.64	3.38–3.60	3.36–3.49	–
$3t_2$	39.3[a]	$6t_2$	–	–	3.36–3.49	2.7[b]
$4a_1$	40.6[a]	$6a_1$ (LUMO)	–	4.57	5.59–5.64	5.5[b]

[a]These values correspond to the energies for the mainlines of the multiply splitted inner-valence structures reported by Perry and Jolly (Ref. 35).

[b]We have re-interpreted the states $\sigma^*(3s)$ and $\sigma^*(3p)$ identified by Friedrich *et al.* (Ref. 23) as the $6a_1$ and $6t_2$ virtual valence orbitals, respectively, in the present notation.

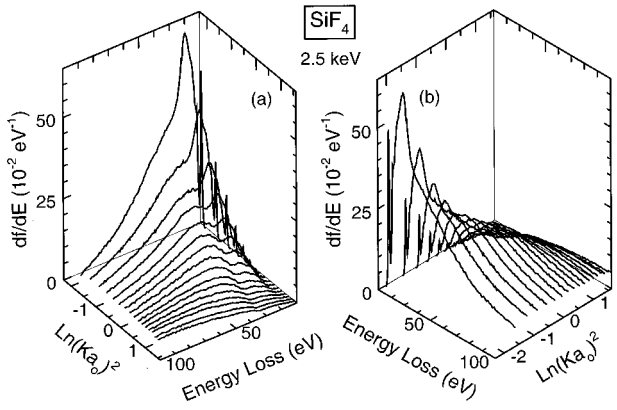

FIG. 2. Bethe surface of the valence shell of SiF_4 determined at 2.5 keV impact energy. Absolute angle-resolved electron energy loss spectra were collected in steps of 0.5° from 1.5° to 9.5° repetitively in sequence scans and have been made absolute by applying the Bethe-sum-rule normalization procedure to the 1.5° spectrum.

similar and are both smaller than that of CCl_4. A smaller valence shell gives rise to a higher average charge density, generally favoring ''close'' collisions (i.e., the impact-scattering region with a larger momentum transfer).

C. GOS profile of preionization-edge valence-shell features

Figure 3 shows selected valence-shell angle-resolved EELS spectra of SiF_4 in the energy loss range of 10–18 eV

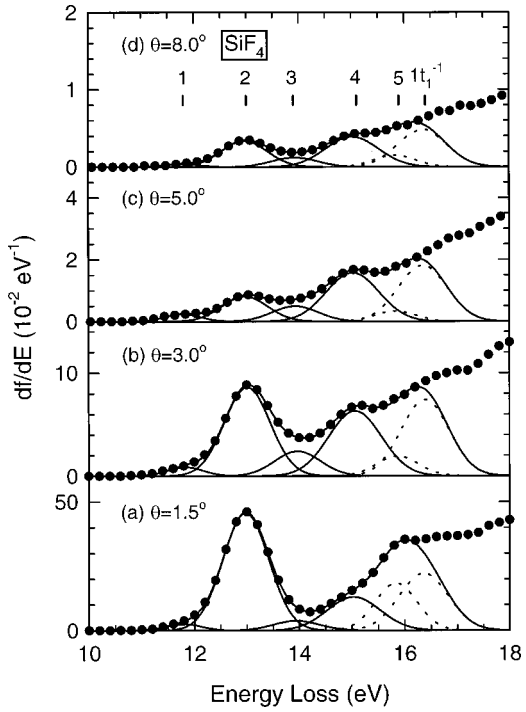

FIG. 3. Absolute angle-resolved electron energy loss spectra of the valence shell of SiF_4 measured at (a) 1.5°, (b) 3.0°, (c) 5.0°, and (d) 8.0°. Six Gaussian line-shapes with the appropriate line-widths are used to estimate the intensities of the preionization-edge structures at 11.8 eV (feature 1), 13.0 eV (feature 2), 13.9 eV (feature 3), 15.1 eV (feature 4), 15.9 eV, and 16.4 eV in a curve-fitting procedure, with the latter two peaks used to simulate the structure near the ionization edge.

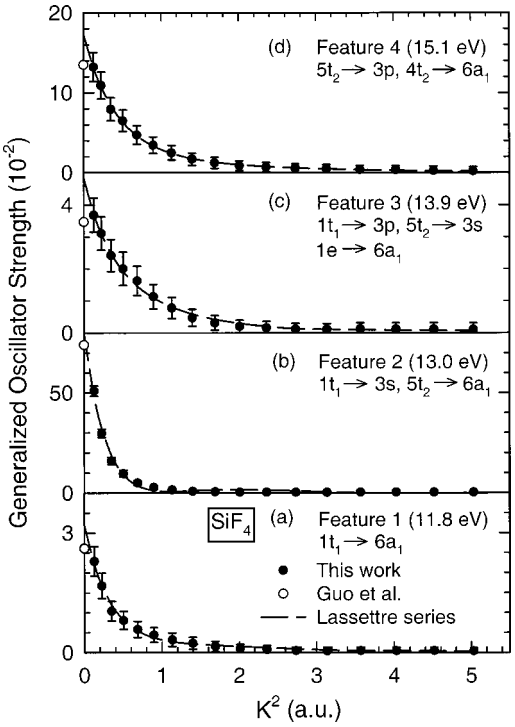

FIG. 4. Absolute generalized oscillator strength as a function of momentum transfer (K) squared for the preionization-edge features at (a) 11.8 eV, (b) 13.0 eV, (c) 13.9 eV, and (d) 15.1 eV in SiF_4. The dashed lines correspond to semiempirical fits using the Lassettre series. The extrapolated values at $K=0$ are compared with the corresponding dipole OSs (open circles) reported by Guo *et al.* (Ref. 27).

collected at 1.5°, 3.0°, 5.0°, and 8.0°, which correspond to momentum transfers of 0.36, 0.71, 1.18, and 1.89 a.u. at 30 eV energy loss, respectively. These spectra have been Bethe–Born-corrected and normalized by the Bethe sum rule as discussed above. Evidently, there is a general reduction in the overall spectral intensity of the entire spectrum with increasing momentum transfer, which is characteristic of the predominantly dipole-allowed nature of the underlying transitions. The nature of the transitions assigned to these low-lying preionization-edge features can be determined more quantitatively by examining their respective GOS profiles. In particular, the preionization-edge features have been fitted with six Gaussian peaks at 11.8 eV (feature 1), 13.0 eV (feature 2), 13.9 eV (feature 3), 15.1 eV (feature 4), 15.9 eV, and 16.4 eV. Only the four lowest-lying peaks are used for estimating the corresponding GOS profiles, while the peaks at 16.4 eV and 15.9 eV are used to better simulate the contributions from the on-set of the ionization edge for the $X(1t_1)^{-1}$ state and the corresponding near-edge structure, respectively. The widths of the Gaussian line-shapes have been estimated from the high-resolution zero-angle EELS spectrum reported by Guo *et al.*,[27] after taking into account our instrumental energy resolution. The GOS of these features are obtained by computing the areas under the respective Gaussian peaks in the absolute angle-resolved EELS spectra collected at different scattering angles. The resulting experimental GOS profiles, shown in Fig. 4, are also fitted semiempirically by using the Lassettre series to extract not only the dipole OS by extrapolation to $K=0$ but also other

TABLE II. Tentative assignments of the observed preionization-edge valence-shell features in the angle-resolved EELS spectra of SiF_4. The term values (in units of eV) for the final-state orbitals are given in round parentheses.

Feature	Energy loss (eV)	Assignment		f_0	f_1/f_0	f_2/f_0	f_3/f_0
		Ref. 20	Ref. 27[a]				
1	11.8	$1t_1 \rightarrow 3s$ (4.64)	$1t_1 \rightarrow 6a_1$ (4.57)	0.032 ±3%	−10.3 ±3%	45.3 ±12%	−61.8 ±15%
2	13.0	$1t_1 \rightarrow 3p$ (3.47) $5t_2 \rightarrow 3s$ (4.62)	$1t_1 \rightarrow 3s$ (3.38) $5t_2 \rightarrow 6a_1$ (4.48)	0.790 ±3%	−13.7 ±7%	60.8 ±12%	−81.3 ±16%
3	13.9	–	$1t_1 \rightarrow 3p$ (2.50) $5t_2 \rightarrow 3s$ (3.60) $1e \rightarrow 6a_1$ (4.22)	0.049 ±4%	−5.2 ±21%	29.6 ±35%	−54.4 ±58%
4	15.1	$1t_1 \rightarrow 3d$ (1.60) $1e \rightarrow 3p$ (3.22)	$5t_2 \rightarrow 3p$ (2.43) $4t_2 \rightarrow 6a_1$ (4.33)	0.178 ±4%	−3.8 ±26%	13.1 ±34%	−15.6 ±67%
α	15.6	–	$1e \rightarrow 3p$ (2.64)				
β	16.0	$5t_2 \rightarrow 3d$ (1.71)	$5t_2 \rightarrow 4s,3d$ (1.56) $4t_2 \rightarrow 3s$ (3.46)				

[a]The dipole oscillator strengths for features 1, 2, 3, and 4 obtained by Guo *et al.* (Ref. 27) are 0.026, 0.740, 0.035, and 0.135, respectively [after applying the appropriate correction discussed by Olney *et al.* (Ref. 2)].

coefficients that are related to linear combinations of various multipole transitions matrix elements.[3,32] These coefficients, along with the proposed assignments by Suto *et al.*[20] and Guo *et al.*,[27] are given in Table II.

Evidently, the maximum at $K=0$ and the general shape of this GOS profile are found to be characteristic of predominantly dipole-allowed transitions for all four preionization-edge features shown in Fig. 4. There are, however, notable differences in the absolute intensities and the shapes, particularly in the half-widths, of these GOS profiles. In particular, the dipole OS values estimated by extrapolation of the GOS profile to zero momentum transfer using the Lassettre fit are in good accord with the corrected zero-angle EELS results reported by Guo *et al.*,[27,2] e.g., 0.032 for feature 1; c.f. 0.026 reported in Refs. 27 and 2, and 0.790 for feature 2, c.f. 0.740 in Refs. 27 and 2. Furthermore, the GOS profiles of features 3 and 4 (with half-widths of $K^2 \sim 0.35$ a.u.) are evidently broader than those of the lower-lying features, especially when compared to the GOS profile of the most intense feature (feature 2) with a half-width of $K^2 \sim 0.2$ a.u. These differences in shapes (corresponding to different distributions of the momentum-transfer components) underline the differences in the nature of the connecting initial states and final states involved in the electronic excitation processes at different energy losses.

The current assignment of the low-lying preionization-edge features in the valence shell of SiF_4, shown in Table II, was developed in part from the photoabsorption studies of the Si $2p$ shell.[23,25] In particular, Suto *et al.* have attributed all of the observed features in the valence shell to Rydberg transitions[20] but noted that their assignment might not be unique, in view of an earlier photoabsorption study of the Si $2p$ region of SiF_4 by Friedrich *et al.*[23] By demonstrating that the lowest-lying pre-edge doublets have considerable molecular characters even for the solid SiF_4 sample, Friedrich *et al.*[23] (and later Bozek *et al.* in their study on a series of fluoromethylsilane compounds[25]) proposed that these pre-edge Si $2p$ features involve transitions to $\sigma^*(3s)$ and $\sigma^*(3p)$ final states (the so-called σ^* resonances). Later, Guo *et al.*[27,28] adapted the use of virtual valence orbital states and provided the most consistent spectral assignment for both the valence and Si $2p$ shells, after consideration of the typical term values and quantum defects for Rydberg orbitals, as well as the multiple-scattering $X\alpha$ results reported by Bozek *et al.*[25] As shown in Table I, the term values of the Rydberg orbitals used in the current assignment by Guo *et al.*[27,28] are evidently transferable from the inner-shell transitions to the valence-shell transitions. On the other hand, the term values of the virtual orbitals derived from the inner-shell transitions are always larger than those obtained from valence-shell transitions due to a larger relaxation effect in the inner shells.[36]

In accord with the assignment made by Guo *et al.*[27] (Table II), the lowest-lying peak at 11.8 eV (feature 1) is attributed to a HOMO→LUMO transition, $1t_1 \rightarrow 6a_1$. Simple MO calculations show that the triply degenerate $1t_1$ orbitals (HOMO) and the doubly degenerate $2e$ orbitals consist essentially of nonbonding (n) F $2p$ atomic orbitals without any Si contribution, while the F $2p$ atomic orbitals in the triply degenerate $5t_2$ orbitals (the next HOMO) are perturbed by weak bonding overlaps with Si $3p$ orbitals. These calculations also show that the lowest unoccupied MO (LUMO) is made up largely of antibonding (σ^*) overlaps between the Si $3p$ and F $2p$ orbitals. Based on symmetry consideration of these essentially $n \rightarrow \sigma^*$ transitions, the $1t_1 \rightarrow 6a_1$ and the $1e \rightarrow 6a_1$ transitions are both electric dipole-forbidden but are magnetic dipole- and electric quadrupole-allowed, respectively, while the electronic transition $5t_2 \rightarrow 6a_1$ is both dipole- and quadrupole-allowed. Although the GOS profile for the lowest-lying preionization-edge feature shown in Fig. 4(a) has the general shape that is commonly associated with a typical dipole-allowed electronic transition, it does not necessarily imply that such a transition cannot be forbidden by symmetry. For example, the GOS profile of the lowest-lying preionization-edge transition in CF_4 observed at 12.6 eV, which is commonly attributed to a $1t_1 \rightarrow 3s$ Rydberg transition formally forbidden by symmetry, does have a maximum at $K=0$ and it follows the general shape of a dipole-allowed profile.[7] A similar observation can also be made for the GOS profile of the $2t_1 \rightarrow 4s$ (and $4p$) transitions (the second

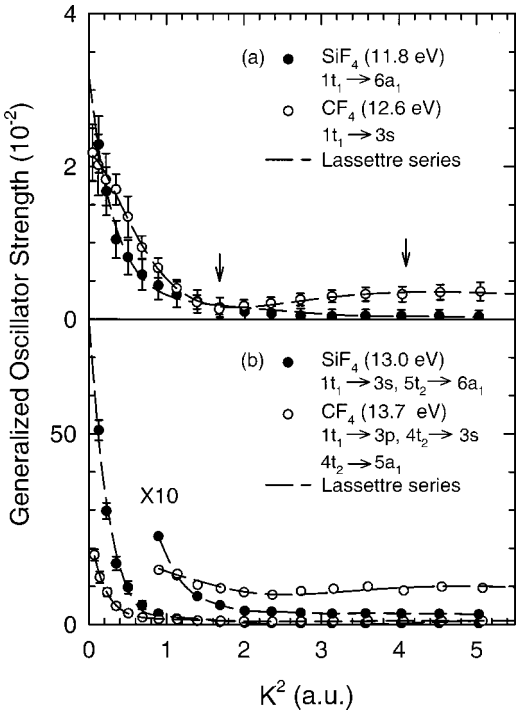

FIG. 5. A comparison of the absolute generalized oscillator strength as a function of momentum transfer (K) squared for (a) the lowest-lying preionization-edge $1t_1 \rightarrow 6a_1$ feature (at 11.8 eV) in SiF_4 and the $1t_1 \rightarrow 3s$ feature (at 12.6 eV) in CF_4 (Ref. 7), and (b) the next lowest-lying feature (at 13.0 eV) in SiF_4 and that (at 13.7 eV) in CF_4 (Ref. 7). The dashed lines correspond to semiempirical fits using the Lassettre series.

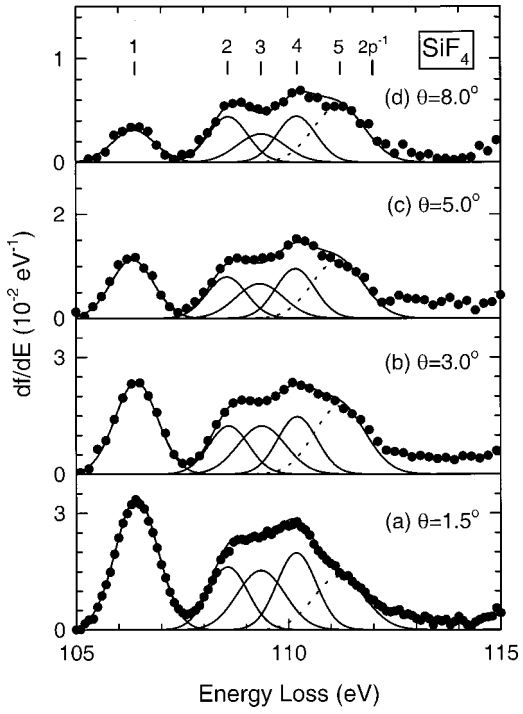

FIG. 6. Absolute angle-resolved electron energy loss spectra for the Si $2p$ region of SiF_4 measured at (a) 1.5°, (b) 3.0°, (c) 5.0°, and (d) 8.0°. Intensities from the valence shell have been removed from the background. Five Gaussian line-shapes with the appropriate line-widths are used in a curve-fitting procedure to estimate the intensities of the structures at 106.4 eV (feature 1), 108.6 eV (feature 2), 109.4 eV (feature 3), and 110.2 eV (feature 4), with the fifth peak at 111.2 eV used to simulate the on-set of the Si $2p$ ionization edge. Only the first four lowest-lying pre-edge features are used to estimate the respective generalized oscillator strength profiles.

lowest-lying preionization-edge feature observed at 8.7 eV) in CCl_4.[7] It is therefore important to realize that of all the GOS profiles reported to date,[14] even though a GOS profile with a maximum at nonzero momentum transfer implies contributions from the underlying nondipole transitions, a monotonically descending GOS profile with a maximum at $K=0$ does not always indicate dipole-allowed transitions. In addition, distortion of the excited states due to Jahn–Teller effects can introduce additional dipole-allowed transition overlaps that may play an important role in the present GOS profile of the lowest-lying preionization-edge feature [Fig. 4(a)].[37] This symmetry breaking mechanism can become quite important in a molecule with a high symmetry such as SiF_4 and it therefore cannot be ruled out.

Figure 5(a) illustrates the subtle differences between the GOS profiles of the $1t_1 \rightarrow 6a_1$ feature in SiF_4 [Fig. 4(a)] and the corresponding lowest-lying preionization-edge feature in CF_4, which has been assigned as a $1t_1 \rightarrow 3s$ Rydberg transition.[7] It is clear that the shapes of the two GOS profiles are quite different from each other, despite the similarity in the overall intensity and the dipole OS. In particular, the GOS profile of the $1t_1 \rightarrow 3s$ Rydberg transition in CF_4 contains a secondary minimum at $K^2=1.7$ a.u. and a secondary maximum at $K^2=4.1$ a.u., in contrast to that of the $1t_1 \rightarrow 6a_1$ discrete excitation in SiF_4. As discussed in our earlier work,[7] given the slowly varying and relatively diffuse nature of the Rydberg orbitals, the spatial distribution of the overlap function generally follows the wave function of the initial-state orbital. These GOS secondary extrema correspond to Fourier components that match the spatial distribution of the overlap function [Eq. (3)] and are ultimately related to the spatial distribution of the nonbonding F $2p$ character of the initial-state orbital wave function of CF_4. In effect, the smaller C–X (X=F or Cl) bond length in CF_4 relative to CCl_4 qualitatively accounts for the larger K values of the GOS extrema for the lowest-lying Rydberg transition in CF_4, when compared with those of the corresponding CCl_4 feature at 8.7 eV.[7] In the case of the lowest-lying preionization-edge feature in SiF_4, the corresponding GOS profile does not appear to contain any discernible secondary extremum. If this SiF_4 feature were to be attributed to a Rydberg transition, as in CF_4 (and CCl_4), secondary extrema are expected to occur at smaller K locations (as in CCl_4) relative to those of CF_4 because of the larger Si–F bond length in SiF_4. The lack of any secondary extrema and the noticeably different shape are therefore consistent with the proposed assignment that the underlying transition does not involve any Rydberg state. The observed differences can be largely attributed to the antibonding σ^*(Si–F) overlap in the final-state orbital $6a_1$.

Figure 4(b) shows the GOS profile of the most intense peak at 13.0 eV (feature 2), which can be attributed to an admixture of $1t_1 \rightarrow 3s$ Rydberg transition and $5t_2 \rightarrow 6a_1$ discrete excitation (Table II). The strongly dipole nature of the $5t_2 \rightarrow 6a_1$ transition, together with the strong low-momentum-transfer component from the (nondipole) $1t_1 \rightarrow 3s$ Rydberg transition, give rise to the strong GOS maxi-

TABLE III. Tentative assignments of the observed pre-edge Si 2*p* features in the angle-resolved EELS spectra of SiF_4. The term values (in units of eV) for the final-state orbitals are given in round parentheses.

Feature	Energy loss (eV)	Assignment		f_0	f_1/f_0	f_2/f_0	f_3/f_0
		Ref. 23[a]	Refs. 28 and 25[a]				
1	106.4	Si $2p_{3/2,1/2}\rightarrow\sigma^*(3s)$ (5.5)	Si $2p_{3/2,1/2}\rightarrow 6a_1$ (5.59, 5.64)	0.052 ±4%	−18.9 ±25%	164.8 ±30%	−509.5 ±63%
2	108.6	Vibrational sideband Si $2p_{3/2}\rightarrow\sigma^*(3p)$ (2.7)	Si $2p_{3/2,1/2}\rightarrow 6t_2,3s$ (3.36, 3.49) Si $2p_{3/2}\rightarrow 7a_1$ (2.88)	0.024 ±4%	−11.3 ±31%	93.8 ±40%	−256.8 ±58%
3	109.4	Si $2p_{1/2}\rightarrow\sigma^*(3p)$ Si $2p_{3/2}\rightarrow 4s$ (2.2)	Si $2p_{1/2}\rightarrow 7a_1$ (2.95) Si $2p_{3/2,1/2}\rightarrow 3p$ (2.34,2.40)	0.029 ±3%	−11.5 ±20%	79.5 ±35%	−195.3 ±58%
4	110.2	Si $2p_{1/2}\rightarrow 4s$ Si $2p_{3/2}\rightarrow 3d$ (1.5)	Si $2p_{3/2}\rightarrow 4s,3d$ (1.79)	0.030 ±4%	−11.3 ±23%	84.1 ±44%	−221.1 ±63%
α	110.7	Si $2p_{1/2}\rightarrow 3d$ Si $2p_{3/2}\rightarrow 5s,4d$ (0.8)	Si $2p_{1/2}\rightarrow 4s,3d$ (1.81)				
β	111.2–111.4	Si$2p_{1/2}\rightarrow 5s,4d$	Si $2p_{3/2,1/2}\rightarrow 4p$ (1.20, 1.11)				

[a]More precise values can be found for various transitions in the original references. The dipole oscillator strengths for features 1 and 2 obtained by Guo *et al.* (Ref. 28) are 0.050 and 0.026, respectively [after applying the appropriate correction discussed by Olney *et al.* (Ref. 2)].

mum at $K=0$. As illustrated in Fig. 5(b), the GOS profile for this intense feature closely resembles that of the corresponding feature in CF_4,[7] which we now reassign as a combination of $1t_1\rightarrow 3p$, $4t_2\rightarrow 3s$, and $4t_2\rightarrow 5a_1$ transitions (all of which are dipole-allowed). Both GOS profiles have half-widths of $K^2\sim 0.2$ a.u. and do not contain any discernible secondary extrema. On the other hand, a broad GOS profile is found for feature 3 at 13.9 eV [Fig. 4(c)], which is assigned as a combination of $1t_1\rightarrow 3p$ and $5t_2\rightarrow 3s$ Rydberg transitions as well as the $1e\rightarrow 6a_1$ discrete electronic excitation. The low-momentum-transfer component (near $K=0$) of the GOS profile shown in Fig. 4(c) can be attributed to the dipole-allowed $1t_1\rightarrow 3p$ and $5t_2\rightarrow 3s$ Rydberg transitions. The dipole-forbidden but quadrupole-allowed $1e\rightarrow 6a_1$ transition may contribute to the higher K component that gives rise to the broad GOS profile. As indicated by the f_0 value in Table II, the dipole OS for feature 3 is similar in magnitude to feature 1 and both are considerably smaller than that of the feature 2 (and feature 4), which reflects the essentially ''nondipole'' characters of the underlying transitions. Finally, a similarly broad GOS profile for feature 4 observed at 15.1 eV is shown in Fig. 4(d). The underlying dipole-allowed $4t_2\rightarrow 6a_1$ transition and dipole-forbidden $5t_2\rightarrow 3p$ Rydberg transition contribute to the low and higher K components of the GOS profile, respectively.

The GOS profiles in Fig. 4 have also been fitted semiempirically by using the Lassettre series [Eq. (5)] to estimate the dipole OS, f_0, and other f_n coefficients. These results for f_0 and the ratios of f_n/f_0 up to $n=3$ are summarized in Table II. In general, these f_n coefficients are related to linear combinations of the respective multipole transition matrix elements and can in principle be used to characterize the nature of the transition itself. It has been shown by Huo that the f_1 term is related to the difference of the square of the quadrupole matrix element and the product of the dipole and octupole matrix elements.[32] For dipole- or octupole-dominated transitions, the f_2 coefficient (in the present expansion to $n=3$) is found to have a positive sign while the odd coefficients, f_1 and f_3, are negative. (The dipole OS f_0 is always positive.) In our earlier work on SF_6, we have shown that the higher-order coefficients of a quadrupole-allowed transition appear to reverse in sign relative to the corresponding coefficients for a dipole-allowed transition.[18] For dipole-allowed transitions and/or nondipole transitions dominated by a strong $K=0$ component, these coefficients may be used to qualitatively describe the overall shapes of the GOS profiles. In particular, the coefficients f_1 and f_2 play an important role on the lower-momentum-transfer region ($K^2<2$ a.u.) while the coefficients f_2 and f_3 govern the higher-momentum-transfer part. In the present case, the f_1/f_0 and f_2/f_0 ratios for the GOS profiles of features 1 and 2 (Table II) are at least double the corresponding ratios for the broader GOS profiles of features 3 and 4 (Fig. 4). A more systematic study is clearly necessary to further exploit the value and validity of this type of semiempirical analysis.

D. GOS profiles of pre-edge Si 2*p* features

Figure 6 shows selected absolute EELS spectra for the pre-edge region of the Si 2*p* shell in SiF_4 at 1.5°, 3.0°, 5.0°,

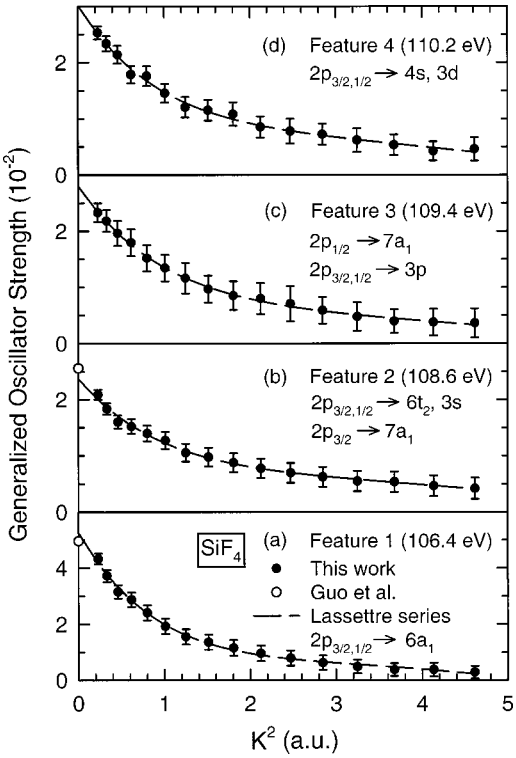

FIG. 7. Absolute generalized oscillator strength as a function of momentum transfer (K) squared for the Si $2p$ pre-edge features at (a) 106.4 eV, (b) 108.6 eV, (c) 109.4 eV, and (d) 110.2 eV in SiF_4. The dashed lines correspond to semiempirical fits using the Lassettre series. The extrapolated values at $K=0$ are compared with the corresponding dipole OS's for features 1 and 2 (open circles) reported by Guo *et al.* (Ref. 28).

and 8.0°, which correspond to momentum transfers of 0.46, 0.76, 1.21, and 1.90 a.u. at 110 eV energy loss, respectively. The background from the valence-shell contribution has been appropriately removed from these inner-shell spectra, which are automatically normalized on an absolute scale because the entire EELS spectra (from the valence shell up to 200 eV) were collected in a self-normalized fashion as discussed above. The intense σ^* resonance at 106.4 eV (feature 1) and three other pre-edge features at 108.6 eV (feature 2), 109.4 eV (feature 3), 110.2 (feature 4) are identified by a Gaussian fitting procedure, employing the natural line widths estimated from the photoabsorption spectrum of Friedrich *et al.*[23] and the high-resolution zero-angle EELS spectrum of Guo *et al.*[28] As with the deconvolution procedure used for the valence shell, a fifth peak at 111.2 eV is used to simulate the near-edge structure. The Si $2p$ pre-edge structure (Fig. 6) is found to be at least an order of magnitude weaker than the valence-shell structure (Fig. 3). In general accord with the inner-shell transitions studied by angle-resolved EELS to date,[10,18] the changes in the overall spectral intensity in the Si $2p$ pre-edge region with momentum transfer is noticeably more gradual and over a more extended momentum-transfer range than that of the valence shell. The intensities of features 1–4 in Fig. 6 are seen to decrease with increasing momentum transfer, which is generally characteristic of the predominantly dipole-allowed nature of the underlying transitions. Except for a general reduction in the overall intensity, there is no discernible difference in the general shape of the electron-impact excitation structure at the larger scattering angles. As noted by Friedrich *et al.*, the early assignments for the Si $2p$ pre-edge features are largely based on transitions to Rydberg orbitals.[23] The subsequent assignments made by Bozek *et al.*[25] and Guo *et al.*[28] incorporated additional virtual valence orbitals, $6a_1$ and $6t_2$, and other mixed virtual/Rydberg orbital, $7a_1$. It should be noted that the so-called $\sigma^*(3s)$ and $\sigma^*(3p)$ identified by Friedrich *et al.*[23] in effect correspond to the $6a_1$ and $6t_2$ virtual valence orbitals, respectively. In the present work, we favor the latter assignment made by Guo *et al.*,[28] particularly given its self-consistency in the term values for various virtual valence and Rydberg orbitals and with the valence-shell assignment. These assignments are summarized in Table III.

Figure 7 shows the GOS profiles for the four fitted Si $2p$ pre-edge features of SiF_4 (identified in Fig. 6), estimated from the areas under the respective Gaussian line-shapes. These GOS profiles are also fitted semiempirically with the Lassettre series to obtain the respective dipole OS and other f_n coefficients shown in Table III. The gradual descending shapes from its maximum at $K=0$ with increasing momentum transfer for these GOS profiles are generally consistent with the spectral assignments that these Si $2p$ pre-edge features are dominated by dipole-allowed transitions. In particular, the most intense σ^* resonance at 106.4 eV (feature 1) corresponds to a well-defined, pre-edge feature attributable to a spin–orbit-splitted pair of Si $2p_{3/2} \rightarrow 6a_1$ and Si $2p_{1/2} \rightarrow 6a_1$ transitions. It should be noted that our instrumental energy resolution is not sufficient to resolve the spin–orbit-splitted pairs of transitions, given the 0.61 eV energy separation between the ionization potentials of the Si $2p_{3/2}$ and Si $2p_{1/2}$ states. Because the final-state orbital $6a_1$ is largely an antibonding σ^* overlap between Si $3s$ and F $2p$ orbitals, the Si $2p_{3/2,1/2} \rightarrow 6a_1$ transitions are therefore dipole-allowed, which gives rise to the strong dipole OS and the characteristic dipole-dominated GOS profile shown in Fig. 7(a). Feature 2 at 108.6 eV [Fig. 7(b)] is assigned as an admixture of $2p_{3/2,1/2} \rightarrow 6t_2$ and $3s$, and $2p_{3/2} \rightarrow 7a_1$ transitions, all of which are dipole-allowed. For both features 1 and 2, there is apparently good agreement between the dipole OS extrapolated from the respective GOS profiles and those reported by Guo *et al.*[28] Feature 3 at 109.4 eV [Fig. 7(c)] is attributed to a mixture of dipole-allowed $2p_{1/2} \rightarrow 7a_1$ and dipole-forbidden $2p_{3/2,1/2} \rightarrow 3p$ transitions, while feature 4 at 110.2 eV [Fig. 7(d)] is assigned as a combination of dipole-allowed $2p_{3/2,1/2} \rightarrow 4s$ and $3d$ Rydberg transitions. Evidently, the GOS profiles for these largely dipole-dominated Si $2p$ pre-edge features are found to be very similar to one another. With the exception of feature 1, Table III shows that the corresponding f_0 and f_n/f_0 $(n=1-3)$ parameters for the other three features are evidently similar in relative magnitude, with essentially the same f_n/f_0 ratios clearly within the experimental uncertainty. Consistent with our earlier inner-shell GOS studies,[10,18] the present work shows that the GOS profiles for the Si $2p$ pre-edge excitation transitions are considerably broader than the valence-shell transitions, which are found to contain sharper variations (as shown in Fig. 4).

It is of interest to compare the GOS profile of the Si $2p$ pre-edge transitions in SiF_4 with the GOS profiles of other

σ^* resonances in other ''cagelike'' molecules, particularly those transitions with the initial state based on an inner-shell orbital of the central atom. Of the limited GOS profiles reported for inner-shell transitions to date,[10,18,38] the GOS profile for the C $1s \rightarrow 7a_1$ (LUMO) and $8t_2$ transitions located at 290.9 eV in CCl_4 appears to parallel the GOS profile of the corresponding Si $2p \rightarrow 6a_1$ [feature 1, Fig. 7(a)] with a very similar shape.[10] Indeed, the GOS profiles for all the C $1s \rightarrow \sigma^*$(C–Cl) (LUMO) transitions in $CF_{4-n}Cl_n$ $(n=1-3)$ also have a similar shape as feature 1.[10] In SF_6, the LUMO $6a_{1g}$ consists of an antibonding σ^* overlap of S 3*s* and F 2*p* atomic orbitals. The corresponding GOS profile for the S $2p \rightarrow \sigma^*$(S–F) resonance is notably ''flatter''[18] than that of Si $2p \rightarrow \sigma^*$(Si–F) resonance [Fig. 7(a)], with the f_1/f_0, f_2/f_0, and f_3/f_0 ratios being 5, 18, and 41 times larger than the corresponding ratios for feature 1 (Table III). Without a more systematic study of these σ^* resonances involving a larger database, it is difficult to assess the usefulness of the present GOS analysis. It is clear, however, that the subtle differences found in the GOS profiles do reflect the intricacy of the underlying transitions and the nature of the connecting initial and final states. There is a serious need for quantitative computation and theoretical investigations of these inner-shell processes.

IV. CONCLUDING REMARKS

Absolute GOS profiles of selected preionization-edge structures of the valence and Si 2*p* shells in SiF_4 have been determined using angle-resolved EELS at 2.5 keV impact energy. In particular, the measured GOS profiles for the lowest-lying preionization-edge, $1t_1 \rightarrow 6a_1$ (HOMO $\rightarrow$LUMO) transition and for three other excitations involving mixed virtual electronic and Rydberg final-state orbitals all have a monotonically descending profile with a maximum at $K=0$ but a different degree of descending slope, generally indicative of dipole-dominated transitions. The GOS profile of the $1t_1 \rightarrow 6a_1$ electronic excitation is clearly different from and does not contain any discernible secondary extrema as the $1t_1 \rightarrow 3s$ Rydberg transition in CF_4, which illustrates the general sensitivity of GOS profiles to the nature of the connecting states of the underlying transitions. In the present work we also show that a formally dipole-forbidden electronic excitation such as the $1t_1 \rightarrow 6a_1$ transition could exhibit a GOS profile with a shape that would normally but as in this case not necessarily imply dipole-dominated transitions. Other symmetry-breaking mechanisms in the excited state including the Jahn–Teller effects may also be operative in introducing dipole-allowed transitions into this feature. The Si 2*p* pre-edge spectrum is dominated by an intense σ^* resonance (Si $2p_{3/2,1/2} \rightarrow 6a_1$) and a broad band with predominantly dipole-allowed Rydberg transitions. Although the corresponding GOS profiles of these Si 2*p* pre-edge features are found to have a shape generally characteristic of predominantly dipole-allowed transitions, the GOS profile for the σ^* resonance appears to be more sharply peaked at $K=0$ than the other Rydberg features. The GOS profiles of these inner-shell transitions are found to be considerably broader than the valence-shell transitions in general. In the present work we show that despite the similarity in the general appearance of the measured GOS profiles, their differences underline the nature of the contributing transitions. Further experimental GOS investigations with a higher energy resolution and especially new complementary theoretical studies involving more quantitative GOS analysis are of great interest to the further development of our current understanding of the intricate electronic structures of ''cagelike'' molecules.

ACKNOWLEDGMENT

This work was supported by the Natural Sciences and Engineering Research Council of Canada.

[1] W. F. Chan, G. Cooper, and C. E. Brion, Phys. Rev. A **44**, 186 (1991).
[2] T. N. Olney, N. M. Cann, G. Cooper, and C. E. Brion, Chem. Phys. **223**, 59 (1997).
[3] E. N. Lassettre and A. Skerbele, in *Methods of Experimental Physics*, edited by D. Williams (Academic, New York, 1974), Vol. 3 (Part B), p. 868.
[4] R. A. Bonham, in *Electron Spectroscopy: Theory, Techniques and Applications*, edited by C. R. Brundle and A. D. Baker (Academic, New York, 1979), Vol. 3, p. 127.
[5] H. Bethe, Ann. Phys. (Leipzig) **5**, 325 (1930); Z. Phys. **76**, 293 (1932).
[6] M. Inokuti, Rev. Mod. Phys. **43**, 297 (1971).
[7] J. F. Ying and K. T. Leung, J. Chem. Phys. **100**, 7120 (1994).
[8] J. F. Ying, C. P. Mathers, K. T. Leung, H. P. Pritchard, C. Winstead, and V. McKoy, Chem. Phys. Lett. **212**, 289 (1993).
[9] J. F. Ying and K. T. Leung, J. Chem. Phys. **101**, 8333 (1994).
[10] J. F. Ying and K. T. Leung, J. Chem. Phys. **101**, 7311 (1994), and references therein.
[11] J. F. Ying and K. T. Leung, J. Chem. Phys. **100**, 1011 (1994).
[12] J. F. Ying and K. T. Leung, J. Chem. Phys. **105**, 2188 (1996).
[13] J. F. Ying and K. T. Leung, Phys. Rev. A **53**, 1476 (1996).
[14] K. T. Leung, J. Electron Spectrosc. Relat. Phenom. **100**, 237 (1999).
[15] X. W. Fan and K. T. Leung, Phys. Rev. A **62**, 062703 (2000).
[16] X. W. Fan and K. T. Leung, Chem. Phys. Lett. (in press).
[17] X. W. Fan and K. T. Leung, J. Phys. B **34**, 811 (2001).
[18] J. F. Ying, C. P. Mathers, and K. T. Leung, Phys. Rev. A **47**, R5 (1993).
[19] J. F. Ying, T. A. Daniels, C. P. Mathers, H. Zhu, and K. T. Leung, J. Chem. Phys. **99**, 3390 (1993).
[20] M. Suto, X. Wang, L. C. Lee, and T. J. Chuang, J. Chem. Phys. **86**, 1152 (1987).
[21] T. Imamura, C. E. Brion, I. Koyano, T. Ibuki, and T. Masuoka, J. Chem. Phys. **94**, 4936 (1991).
[22] W. Hayes and F. C. Brown, Phys. Rev. A **6**, 21 (1972).
[23] H. Friedrich, B. Pittel, P. Rabe, W. H. E. Schwarz, and B. Sonntag, J. Phys. B **13**, 25 (1980).
[24] T. A. Ferrett, M. N. Piancaselli, D. W. Lindle, P. A. Heimann, and D. A. Shirley, Phys. Rev. A **38**, 701 (1988).
[25] J. D. Bozek, G. M. Bancroft, and K. H. Tan, Chem. Phys. **145**, 131 (1990).
[26] R. Püttner, M. Domke, K. Schulz, and G. Kaindl, Chem. Phys. Lett. **250**, 145 (1996).
[27] X. Guo, G. Cooper, W.-F. Chan, G. R. Burton, and C. E. Brion, Chem. Phys. **161**, 453 (1992).
[28] X. Guo, G. Cooper, W.-F. Chan, G. R. Burton, and C. E. Brion, Chem. Phys. **161**, 471 (1992).
[29] M. Inokuti, J. L. Dehmer, T. Baer, and J. D. Hanson, Phys. Rev. A **23**, 95 (1981), and references therein.
[30] J. A. Wheeler and J. A. Bearden, Phys. Rev. **46**, 755 (1934).
[31] E. N. Lassettre, J. Chem. Phys. **43**, 4479 (1965); M. A. Dillon and E. N. Lassettre, *ibid.* **62**, 2373 (1975). See also M. A. Dillon, M. Inokuti, and Z. W. Wang, Radiat. Res. **102**, 151 (1985).
[32] W. M. Huo, J. Chem. Phys. **71**, 1593 (1979).
[33] A. E. Jonas, G. K. Schweitzer, F. A. Grimm, and T. A. Carlson, J. Electron Spectrosc. Relat. Phenom. **1**, 29 (1972/1973).

[34] B. W. Yates, K. H. Tan, G. M. Bancroft, L. L. Coatsworth, and J. S. Tse, J. Chem. Phys. **83**, 4906 (1985).
[35] W. B. Perry and W. L. Jolly, J. Electron Spectrosc. Relat. Phenom. **4**, 219 (1974).
[36] M. B. Robin, *Higher Excited States of Polyatomic Molecules* (Academic, New York, 1985), Vol. 3.
[37] E. N. Lassettre, in *Chemical Spectroscopy and Photochemistry in the Vacuum-Ultraviolet*, edited by C. Sandorfy, P. J. Ausloos, and M. B. Robins (Reidel, Dordrecht, 1974), p. 43.
[38] J. T. Francis, C. C. Turci, T. Tyliszczak, G. G. B. de Souza, B. Kosugi, and A. P. Hitchcock, Phys. Rev. A **52**, 4665 (1995).